Electronic Preprint for Journal of Information Processing Vol.28

Regular Paper

A Novel Method for Reconstructing CT Images in GATE/GEANT4 with Application in Medical Imaging: A Complexity Analysis Approach

Neda Gholami[1,a)] Mohammad Mahdi Dehshibi[2,b)] Andrew Adamatzky[3]
Antonio Rueda-Toicen[4] Hector Zenil[4,5,6] Mahmood Fazlali[7] David Masip[2]

Received: June 7, 2019, Accepted: November 7, 2019

Abstract: For reconstructing CT images in the clinical setting, 'effective energy' is usually used instead of the total X-ray spectrum. This approximation causes an accuracy decline. We proposed to quantize the total X-ray spectrum into irregular intervals to preserve accuracy. A phantom consisting of the skull, rib bone, and lung tissues was irradiated with CT configuration in GATE/GEANT4. We applied inverse Radon transform to the obtained Sinogram to construct a Pixel-based Attenuation Matrix (PAM). PAM was then used to weight the calculated Hounsfield unit scale (HU) of each interval's representative energy. Finally, we multiplied the associated normalized photon flux of each interval to the calculated HUs. The performance of the proposed method was evaluated in the course of Complexity and Visual analysis. Entropy measurements, Kolmogorov complexity, and morphological richness were calculated to evaluate the complexity. Quantitative visual criteria (i.e., PSNR, FSIM, SSIM, and MSE) were reported to show the effectiveness of the fuzzy C-means approach in the segmenting task.

Keywords: Complexity, CT image, FCM, GATE/GEANT4, Hounsfield Unit, Pixel-based Attenuation Matrix

1. Introduction

Clinical imaging techniques are essential components of medical diagnostics. Computed tomography (CT) is one of the most widely used medical imaging methods in which attenuating properties are used in calculating Hounsfield Unit (HU) to visualize objects. Scanner types, projection systems, and reconstruction algorithms have impacts on CT scanners' output, where modifying scanner type and projection systems need substantial investment in physical development [4]. Therefore, many studies tried to contribute towards reconstruction algorithms for better scanning of different phantoms [7].

CT imaging is an inverse problem in which analytical and iterative reconstruction methods are used to visualize images [10]. These reconstruction methods founded on the use of attenuation coefficients and the 'effective energy' in the total X-ray spectrum. However, using effective energy instead of the whole range causes a decline in the contrast level and can introduce artifacts. Several image enhancement techniques have been proposed to solve these issues. Chen et al. [2] developed a low-rank and sparse decomposition framework to simultaneously reconstruct and segment tissues obtained from a dynamic Positron-emission tomography (PET). Since PET has a relatively low spatial resolution and high level of noise, they proposed a mixed CT and PET architecture to characterize tissue elements reliably. Xu et al. [20] proposed an image reconstruction model, regularized by edge-preserving diffusion and smoothed for limited-angle CT.

Chen et al. [3] developed *a prior* contour-based total variation method to enhance the edge information in compressed sensing reconstruction for cone-beam computed tomography (CBCT). Although CBCT has been widely used in radiation therapy for onboard target localization, they showed that using this method in reconstruction will result in over-smoothing the edge information. Wang et al. [19] proposed a method for reconstructing CT data in limited-angle CT devices. To solve the ill-posed problem, they proposed an iterative re-weighted method, in which the re-weighted technique is incorporated into the idea of the total anisotropic variation. In this way, they could approximate the most direct measure of L_0 norm sparsity.

Gholami [9] created an attenuation map by applying the inverse HU to CT images reconstructed in 70 keV. Although quantizing 'effective energy' could provide a better reconstruction, they neutralized the effect of HU by using the inverse HU and did not consider the statistical distribution of the source photon flux for the quantization. Following their idea, we proposed a novel

1 Pattern Research Center, Tehran, Iran
2 Department of Computer Science, Multimedia and Telecommunication, Universitat Oberta de Catalunya, Barcelona, Spain
3 Unconventional Computing Laboratory, University of the West of England, Bristol, UK
4 Algorithmic Nature Group, LABORES for the Natural and Digital Sciences, Paris, France
5 Algorithmic Dynamics Lab, Unit of Computational Medicine, SciLifeLab, Centre for Molecular Medicine, Department of Medicine Solna, Karolinska Institute, Stockholm, Sweden
6 Oxford Immune Algorithmics, Oxford University Innovation, Oxford, UK
7 Department of Computer Science, Shahid Beheshti University, G.C., Tehran, Iran
a) gholami@iranprc.org
b) mdehshibi@uoc.edu

post-processing algorithm to cover more energy range in the total X-ray spectrum and establish a trade-off between accuracy and computational cost. We quantized the X-ray spectrum into 13 intervals, ranged from 10 to 140 keV. To validate the proposed method, we created a phantom in the GATE/GEANT4 environment consisting of the skull, rib bone, and lung tissues surrounded by water. This phantom was then irradiated in a double-wedge way by a fan-beam X-ray. To calculate the effective energy of each interval, we used the mean energy of each interval and its associated water attenuation coefficient [12], see Eq. (1):

$$HU = \frac{\mu - \mu_w}{\mu_w} \times 1000 \tag{1}$$

where μ is the attenuation coefficient, and μ_w is the water attenuation coefficient. A pixel-based attenuation matrix (PAM) was then created by applying the back-projection method. PAM was used to weight the value of HU and to normalize photon flux. We observed that the proposed post-processing method could increase the contrast of target tissue in the CT image and subsequently ease the segmentation task. The rest of this paper is organized as follows: Section 2 describes the proposed post-processing method. Experimental results are discussed in Section 3, and the conclusion is drawn in Section 4.

2. Methodology

Imaging environment in the GATE/GEANT4 is an air cube that is 50 cm on each side spanned in {(−25, 25, 25), (25, −25, 25), (25, 25, −25), (−25, −25, 25), (−25, 25, −25), (25, −25, −25), (25, 25, 25), (−25, -25, −25)}. This cube defines our coordinate system where the rest of the components will be defined with respect to this coordinate system. The source is a fan beam CT geometry with the size of 0.5×0.5 mm^2, placed in (0, 0, 150). The scanner consists of 30×16 cubic cell detectors (0.5×0.5×1 mm^3) made of Lutetium, Silicon, and Oxygen. The phantom is a cylinder with a radius of 5 mm and the height of 6 mm consisting of the skull, rib bone, and lung tissues (1×1×2 mm^3) surrounded by water. Density of tissues are 0.26, 1.92, and 1.61 g/cm^3, respectively. Structure of phantom and positions of tissues are shown in **Fig. 1**.

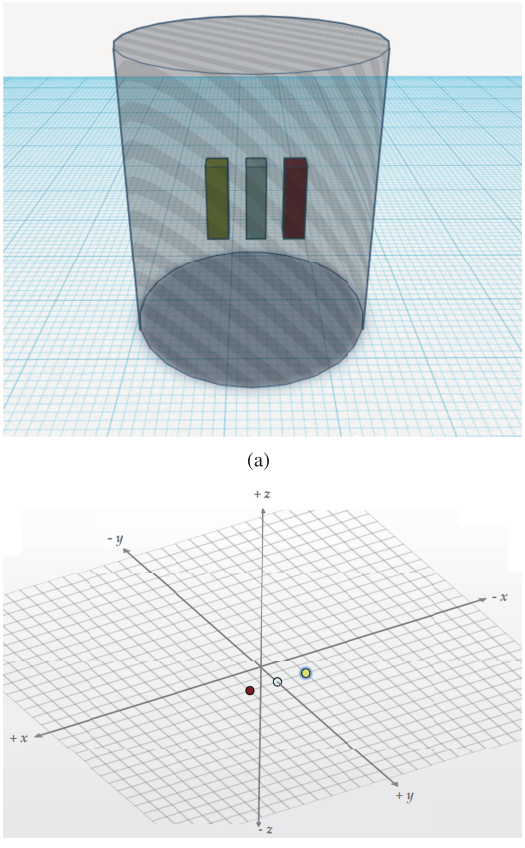

(a)

(b)

Fig. 1 (a) Constructed phantom in GATE. (b) Rib bone (red), Lung (white), and Skull (yellow) tissues are placed in (2, 2, 0), (0, 2, 0), and (−2, 2, 0), respectively.

GATE, the Geant4 Application for Tomographic Emission developed by the international OpenGATE collaboration, has a dominant utilization in numerical simulations in medical imaging and radiotherapy. It takes advantage of the (1) well-validated

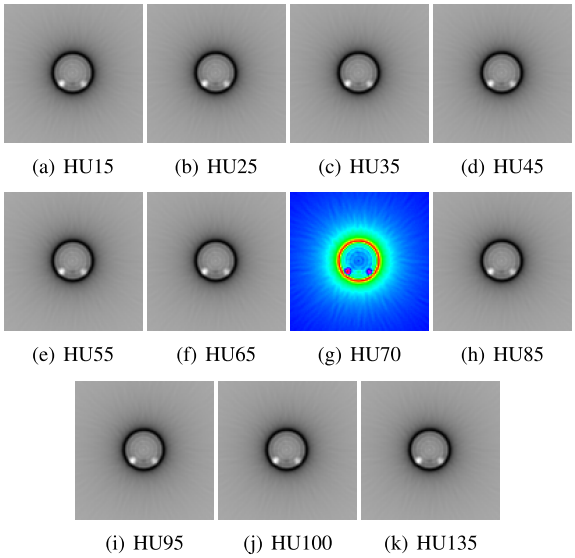

(a) HU15 (b) HU25 (c) HU35 (d) HU45

(e) HU55 (f) HU65 (g) HU70 (h) HU85

(i) HU95 (j) HU100 (k) HU135

Fig. 2 CT images (200 × 200) in energy levels of 15–135 keV (a-k). CT image in the energy level of 70 keV (g) is illustrated in HSV color map to make differences distinguishable visually.

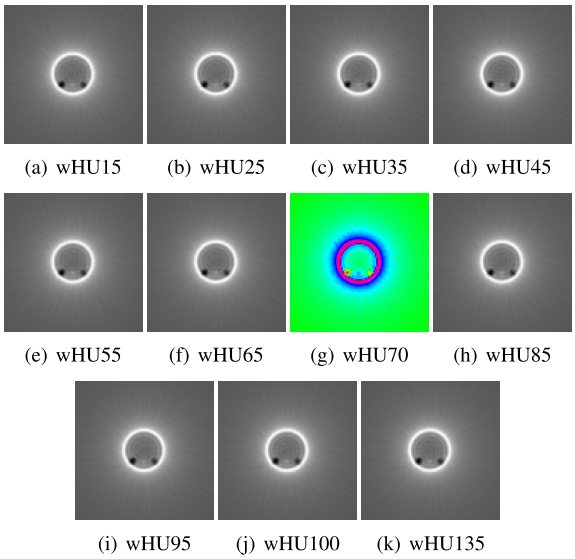

(a) wHU15 (b) wHU25 (c) wHU35 (d) wHU45

(e) wHU55 (f) wHU65 (g) wHU70 (h) wHU85

(i) wHU95 (j) wHU100 (k) wHU135

Fig. 3 Post-processed CT images (200 × 200) in energy levels of 15–135 keV (a-k). Image in the energy level of 70 keV (g) is illustrated in HSV color map to make differences distinguishable visually.

physics models, (2) geometry description, and (3) visualization with 3D rendering tools to facilitate simulations of Emission Tomography (Positron Emission Tomography - PET and Single Photon Emission Computed Tomography - SPECT), Computed Tomography (CT), Optical Imaging (Bioluminescence and Fluorescence) and Radiotherapy experiments [11]. They compose an object-oriented, modular set of components written in C++ which we configured it as follow:

```
/gate/source/addsource xraygun gps
/gate/source/verbose 0
/gate/source/xraygun/setactivity 100000000. Becquerel
/gate/source/xraygun/gps/verbose 0
/gate/source/xraygun/gps/particle gamma
/gate/source/xraygun/gps/energytype user
/gate/source/xraygun/gps/hist/type energy
/gate/source/xraygun/gps/histname arb
/gate/source/xraygun/gps/emin 10.00 keV
/gate/source/xraygun/gps/emax 140.00 keV
```

The proposed post-processing method aims at increasing the contrast of tissues in the reconstructed image through the steps of Algorithm 1:

Algorithm 1: Proposed post-processing algorithm.

Input :
PAX ← projected attenuation X-ray.
W ← water attenuation coefficient.
F ← photon flux value.

PAM = iradon(PAX)
Form intervals as:
X ← {(12-17), (18-27), (28-37), (38-47), (48-57), (58-67), (60-72), (68-80), (78-87), (81-95), (88-100), (98-105), (130-150)}
Take Kolmogorov-Smirnov test to find the best distribution that fits X:
$F_n(x) = \frac{1}{n}\sum_{i=1}^{n} I_{[\infty,x]}(X_i)$,
$D_n = \sup_x |F_n(x) - F(x)|$
where $F(x)$ is the hypothesis distribution, $F_n(x)$ is the cumulative distribution function, and $I_{[\infty,x]}(X_i)$ is the indicator function, equals to 1 if $X_i \leq x$ and equals to 0 otherwise.
Calculate the "effective energy":
$\mu_w \leftarrow \{\mu_{w_i} \mid \mu_{w_i} = \mathrm{E}[x], \quad x \in \mathrm{X_i}, 1 \leq i \leq 13\}$
$mF = \sum_{i=1}^{13} F_i$
$i = 1$
while $i \leq 13$ **do**
  $HU_i = \frac{PAM - \mu_{w_i}}{\mu_{w_i}} \times 1000$,
  $q_i = \frac{F_i}{mF}$,
  $wHU_i = q_i \times HU_i$
end
Output: post-processed HU → wHU

Figure 2 and **Fig. 3** show the output of CT scanner before and after applying the post-processing approach, respectively. In order to visually distinguish differences between standard and post-processed CT images, we used HSV color map in illustrating reconstructed images in 70 keV (see Fig. 2 (g) and Fig. 3 (g)). As is evident, not only the proposed post-processing method can reduce associated artefacts but also can make CT images more ideal for the task of segmentation.

3. Experimental Results

To evaluate the post-processing method, we conducted visual and complexity experiments where entropy measurements, Kolmogorov complexity, morphological richness, and quantitative visual criteria (i.e., PSNR, FSIM, SSIM, and MSE) were calculated. Constructed phantom in GATE/GEANT4 environment made of skull, rib bone, and lung tissues surrounded by water. The radiation range of fan-beam X-ray changed from 10 to 140 keV in a way that could cover double-wedge.

Probability density functions were calculated for both CT and post-processed CT images to quantitatively compare them. Let a simulated image is represented by the histogram of indexed values in the range of $I(u,v) \in [-\infty, \infty]$. It contains exactly K entries which are defined by $h(i) = \mathbf{card}(\{(u,v)|I(u,v) = i\})$. To compare CT and post-processed CT images (obtained as n independent realizations of a bounded probability distribution with smooth density), we combined ranges of indexed values into histogram columns following Scott's normal reference rule [16]. **Figure 4** (a) and Fig. 4 (b) show aligned indexed value of all reconstructed CT images before and after applying post-processing approach, respectively. It is evident that bins in the histogram of post-processed CT images (Fig. 4 (b)) have relatively less overlap and bigger distribution compared to Fig. 4 (a). Hence, segmenting a CT image by using shape, clustering, or entropy-based method is more straightforward. Moreover, mounting the proposed post-processing approach into imaging software gives an expert radiologist the flexibility to modify the energy level for reaching the best tissue differentiation in the final CT image.

3.1 Complexity Analysis

In this study, we used Kolmogorov estimation, which is an approximation to the algorithmic complexity. Kolmogorov complexity (K) can quantify the randomness content in both CT and post-processed CT images. $K(x)$ is defined as the length (in bits) of the smallest computer program that can reproduce the object

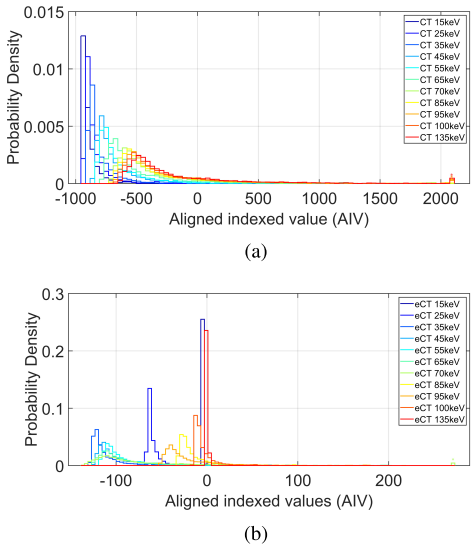

Fig. 4 Aligned indexed value of all reconstructed CT images from HU scale (a) before applying post-processing, (b) after applying post-processing.

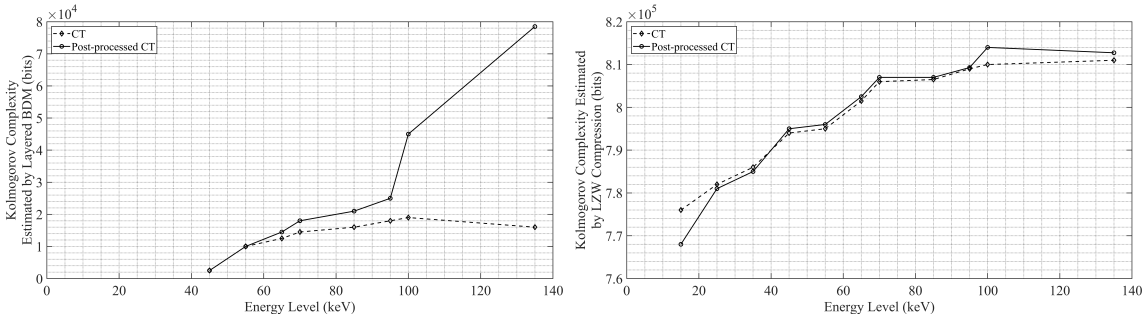

Fig. 5 Estimations of Kolmogorov complexity. (a) Kolmogorov complexity estimated by the layered BDM in CT images and post-processed CT images, Spearman $\rho = 0.972$, *p-value* $= 5.58 \times 10^{-7}$. (b) Kolmogorov complexity estimated by LZW in CT images and processed CT images, Spearman $\rho = 0.98$, *p-value* $= 8.4 \times 10^{-8}$.

(x) when it runs on a Universal Turing Machine U. Since K is semi-computable, compression algorithms can utilize to approximate it. However, it has been shown [21] that compression algorithms are entropy rate approximations. Therefore, to consider algorithmic content, we proposed an algorithmic probability-based approach to estimate K.

Algorithmic probability, which is inversely proportional to K, is the probability of an object x to be produced by a Universal Turing Machine. It can be empirically estimated from the output frequency of small Turing machines using Coding theorem (CTM) and Block decomposition methods (BDM) [17]. To calculate K [15], we considered layers in which images are quantized and binarized in q digital levels. This quantization is prior to the aggregation of CTM values, where each layer gets decomposed.

Algorithm 2: Layered Block Decomposition

```
   // CTM is a hash-table with binary 2D blocks as keys,
   // Output is the Kolmogorov complexity
1
2  Function LayeredBDM(grayImage, CTMs, blockSize, blockOffset, q) is
3      - Quantize image in q digital levels and binarize in q digital layers
4      grayImage ⟵ quantize(grayImage, q) blocksList ⟵ {} for i in 1
       to q do
5          binImage ⟵ binarize(grayImage, q)
6          blocks ← partition (binImage, blockSize, blockOffset)
7          blocksList.append(blocks)
8      end
9      - Occurrence of all binary blocks in all layers stores in a hash table
       with the blocks as keys blockHT(blocks:blockCount) ⟵
       countBlocks(blockList)
10     l-BDM ← CTMs(keys(blockHT)) + log2(values(blockHT))
11     return l-BDM
12 end
```

Figure 5 (a) shows the estimations of BDM to K for CT and post-processed CT images using the layered BDM where $q = 256$. Figure 5 (b) shows the KC estimation obtained by the lossless compression algorithm Lempel-Ziv-Welch (LZW) for comparison. Both Fig. 5 (a) and Fig. 5 (b) show an almost monotonic increase in complexity when the energy level increases. For energy levels below 65 keV in Fig. 5 (a), a small difference in KC between CT and post-processed CT is evident. We performed the Spearman's rank correlation test between the KC values obtained with layered BDM and compression length. In CT data, this test gives $\rho = 0.96$ with p-value $= 1.91 \times 10^{-6}$ and in the post-processed CT data, it results in $\rho = 0.97$ with p-value $= 5.32 \times 10^{-7}$. These results indicate that the layered BDM is more sensitive to morphological changes in the images than the ones obtained from lossless compression.

The benefit of utilizing entropy in the context of complexity is that it only considers the probability of observing a specific event. Therefore, it does not express any interpretation of the meaning of the events themselves. In this study, we calculate approximate, conditional, corrected conditional, sample, and fuzzy entropy measurements to show the complexity of the CT (**Fig. 6** (a)) and processed CT (Fig. 6 (b)) data. Approximate entropy (ApEn) [13] quantifies the amount of regularity and the unpredictability of fluctuations in reconstructed CT images. It modifies an exact regularity statistic, i.e., Kolmogorov-Sinai entropy, to handle the system noise. To address the complexity of reconstructed CT images from different perspectives, we also calculated the following entropy measures.

- We measured conditional entropy [5] to quantify the amount of information needed to describe the outcome of CT images in different energy levels.
- We calculated corrected conditional entropy (CCEn) to measure the information content with respect to the minimum value of Eq. (2) function.

$$\begin{aligned} \mathrm{CCEn}(L) &= \hat{E}(L/l-1) + E_c(L) \\ E_c(L) &= \mathrm{perc}(L).\hat{E}(1) \end{aligned} \tag{2}$$

  where $\hat{E}(L/l-1)$ represents the estimate of Shannon entropy in a $L/L-1$-dimensional phase space. perc(L) is the percentage of single points in the L-dimensional phase space, and $\hat{E}(1)$ is the estimated value of Shannon entropy for $L = 1$.
- Sample entropy (SEn) [14] is a modification of approximate entropy with two advantages over ApEn including independence from data length and a relatively trouble-free implementation. As self-matching is not included in Sample entropy, actual interpretation about the irregularity of signals is possible. For a given embedding dimension m, tolerance r and number of data points N, SEn is calculated by Eq. (3).

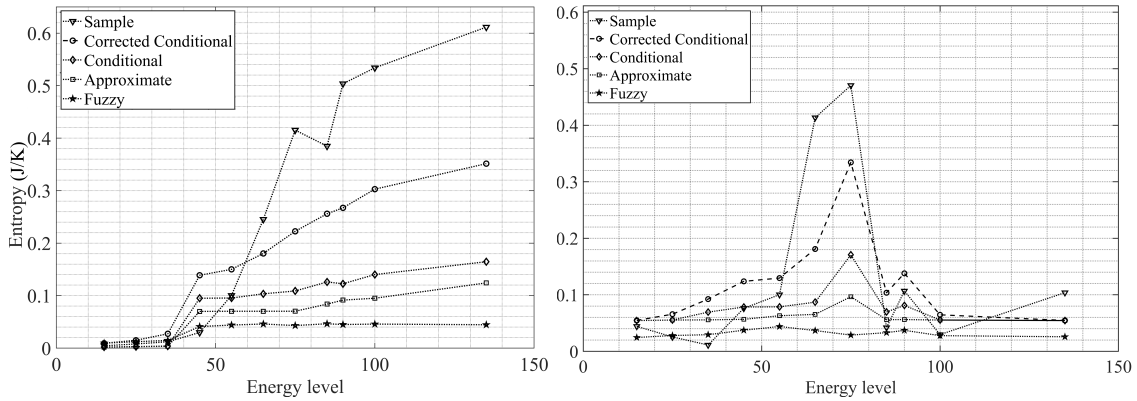

(a) CT (b) Post-processed CT

Fig. 6 Approximate, Conditional, Corrected Conditional, Sample, and Fuzzy entropy measurements for (a) CT images and (b) post-processed CT in different energy levels.

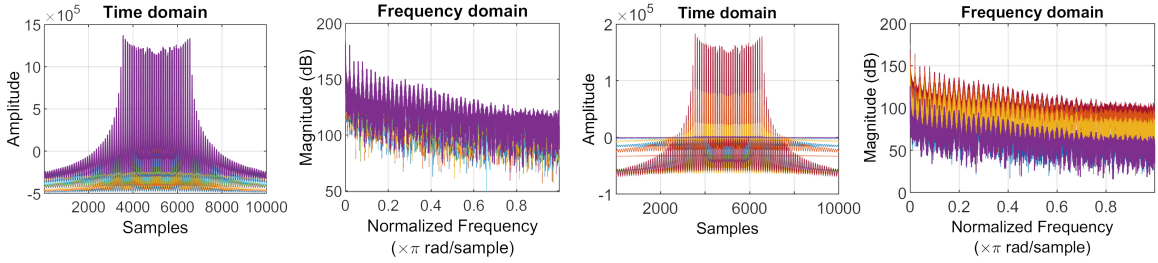

(a) (b)

Fig. 7 Power spectrum of the entropy of the calculated morphological richness. (a) CT images, (b) processed CT images. Each color is associated with an energy level.

$$\mathrm{SEn} = -\log \frac{A}{B}, \tag{3}$$

where A is a number of template vector pairs (e.g., $d[X_{m+1}(i), X_{m+1}(j)] < r$) with length of $m+1$ and B is a number of template vector pairs ($d[X_m(i), X_m(j)] < r$) with length of m.

- Fuzzy entropy (FEn) estimates the short-length data without restricting validity by the parameter value. It evaluates global deviations from the type of ordinary sets and is resistant to noise and jamming phenomena (Eq. (4)).

$$\begin{aligned} \mathrm{FEn}(m,n,r,N) &= \ln \phi^m(n,r) - \ln \phi^{m+1}(n,r), \\ \phi^m(n,r) &= \frac{1}{N-m} \sum_{i=1}^{N-m} [\frac{1}{N-m-1} \sum_{j=1, j\neq i}^{N-m} D_{ij}^m] \end{aligned} \tag{4}$$

where m and r are the dimensions of phase space and similarity tolerance, respectively, n is the gradient of the exponential function, N is the number of data, and D is the similarity degree.

Lower entropy means that the CT image is more homogeneous. From Fig. 6 (b), we can see that for different energy levels (except for 70 keV) the entropy level of post-processed CT images are relatively the same while the entropy in Fig. 6 (a) monotonically increased. Therefore, designing an analytical approach for raw CT images involves a trade-off between the amount of information and the number of components that characterize the image. The sharp entropy change in Fig. 6 (b) echoes the results of previous studies (e.g., Ref. [1]) where energy level of 70 keV was used to form the attenuation map and get the best reconstruction results. Indeed, at this energy level, we have the maximum amount of information which was proven as the appropriate energy level for x-ray based medical image reconstruction.

3.2 Visual analysis

In this section, we show the performance of the proposed post-processing approach using morphological richness analysis [18] and fuzzy c-means (FCM) [8] based segmentation.

Morphological richness (MR) represents the number of different configurations of 3×3 blocks divided by the number of all possible configurations (2^9). To amplify changes in the restructuring of reconstructed images, we calculated the power spectrum of morphological richness using Eq. (5), where $F_T(\omega)$ is the Fourier transform of the signal (vectorized CT image) in period T. The power spectrum itself is a Fourier transform of the autocorrelation function. The auto-correlation function represents the relationship of long and short-term correlation within the signal itself (refer to Eq. (6)).

$$S_f(\omega) = \lim_{T\to\infty} \frac{1}{T} |F_T(\omega)|^2. \tag{5}$$

$$< f(t), f(t+\tau) >= \frac{1}{2\pi} \int_0^\infty S_f(\omega) e^{-j\omega t} d\omega \tag{6}$$

The results of our analysis are illustrated in **Fig. 7**. Amplitude and "dominating frequencies" differentiations are evident in processed CT images which imply that analyzing processed CT images would bring more information. Solid and slow components in the frequency domain imply that there is a high correlation between macro-structures, while extreme and fast oscillations imply

Table 1 Evaluation criteria of FCM applied to both CT and post-processed CT images.

	Post-processed CT				CT			
Energy level (keV)	**FSIM**	**SSIM**	**MSE**	**PSNR**	**FSIM**	**SSIM**	**MSE**	**PSNR**
15	0.95	0.95	3.23	−5.10	0.94	0.94	11.82	−10.72
25	0.91	0.91	1.24	−0.94	0.90	0.90	9.14	−9.61
35	0.97	0.97	11.53	−10.62	0.94	0.94	11.62	−10.65
45	0.93	0.93	9.21	−9.64	0.89	0.89	5.54	−7.43
55	0.95	0.95	0.88	0.50	0.94	0.94	3.99	−6.01
65	0.91	0.91	8.27	−9.17	0.89	0.89	3.17	−5.01
70	1.00	1.00	0.00	−9.91	0.93	0.93	1.71	−2.33
85	0.94	0.94	11.62	−10.65	0.90	0.90	6.70	−8.26
95	0.95	0.95	3.85	−5.86	0.95	0.95	0.88	0.50
115	0.88	0.88	9.65	−9.84	0.90	0.90	3.18	−5.03
135	0.91	0.91	5.84	−7.66	0.93	0.93	1.71	−2.33

correlation in the micro-structures.

Image segmentation plays the essential role in medical image processing [6]. Fuzzy c-means (FCM) is one of the popular clustering algorithms [8] used in medical image segmentation. However, FCM is highly vulnerable to noise which is an unavoidable element in reconstructing CT images. To show the performance of the proposed post-processing approach, we applied FCM segmentation to both conventional CT and processed CT images. FCM minimizes an object function by partitioning a finite collection of n elements $X = \{\mathbf{x}_1, \ldots, \mathbf{x}_n\}$ into a collection of c fuzzy clusters with respect to some given criterion. FCM returns a list of c cluster centers $C = \{\mathbf{c}_1, \ldots, \mathbf{c}_c\}$ and a partition matrix $W = w_{i,j} \in [0,1],\ i = 1, \ldots, n,\ j = 1, \ldots, c$, where each element, w_{ij}, tells the degree to which element, $\mathbf{x}_i$, belongs to cluster $\mathbf{c}_j$. The objective function can be defined by Eq. (7).

$$\begin{aligned} &\arg\min_{C} \sum_{i=1}^{n} \sum_{j=1}^{c} \| x_i - c_i \|^2, \\ &w_{ij} = \frac{1}{\sum_{k=1}^{c} \left(\frac{\|x_i - c_j\|}{\|x_i - c_k\|} \right)^{\frac{2}{m-1}}} \end{aligned} \tag{7}$$

To evaluate FCM, we calculated four measurements (Eq. (8)) including Peak-value signal-to-noise ratio (PSNR), feature-similarity (FSIM) index, Structural Similarity (SSIM) index, and Mean Square Error (MSE).

$$\begin{aligned} \mathrm{PSNR}(I_T, I_R) &= 10 \cdot \log_{10} \left(\frac{MAX_{I_T}^2}{MSE} \right), \\ \mathrm{FSIM}(I_T, I_R) &= \frac{\sum_{x \in \Omega} S_L(x) \cdot PC_m(x)}{\sum_{x \in \Omega} PC_m(x)}, \\ \mathrm{SSIM}(I_T, I_R) &= \frac{(2\mu_{I_T}\mu_{I_R} + c_1)(2\sigma_{I_T, I_R} + c_2)}{(\mu_{I_T}^2 + \mu_{I_R}^2 + c_1)(\sigma_{I_T}^2 + \sigma_{I_R}^2 + c_2)}, \\ \mathrm{MSE}(I_T, I_R) &= \frac{1}{mn} \sum_{i=0}^{m-1} \sum_{j=0}^{n-1} \left[I_T(i,j) - I_R(i,j) \right]^2. \end{aligned} \tag{8}$$

where I_T is the target image with the size of $m \times n$, PC_m is the weighting factor for $S_L(x)$ which is the overall similarity between I_T and a reference image I_R, μ is the mean of the image, σ^2 is the variance of image, σ_{I_T, I_R} is the covariance of I_T and I_R, and c_1 and c_2 are two variables to stabilize the division with weak denominator. In our experiments we set $c_1 = (0.01 \times 2{,}155)^2$ and $c_2 = (0.03 \times 2{,}155)^2$. The quantitative measurements, showed in **Table 1**, will help us to draw the following conclusion remarks:

(1) We can see sharp changes in entropy measures for both CT and post-processed CT images in the range of 50-90 keV. The reason for these sharp changes is the slight tissue differentiation between the phantom's components and water. Moreover, this change agrees with the results of previous studies (e.g., Ref. [1]) where the maximum amount of information shows the appropriateness of this energy level for x-ray based medical image reconstruction.

(2) Quantitative measurements show that the post-processing algorithm improved the quality of CT images and decrease the noise level. Therefore, with a lower degree of irradiation and less tissue damage, we can reach better tissue discrimination.

(3) Although reconstructing CT images is usually made in the energy level of 70 keV, results of our experiments prove that working on CT images in different energy levels is possible, either by applying the proposed post-processing method or physical modification. In this way, an expert can reach better tissue discrimination in CT images.

4. Conclusion

We presented an algorithmic protocol of increasing tissue discrimination using post-processing of CT images. A phantom consisting of the skull, rib bone, and lung tissues was created and irradiated in GATE/GEANT4 to validate the proposed method. By quantizing the total X-ray spectrum into irregular intervals, we could have different Sinograms with different levels of tissue discrimination. In each energy interval, the mean was considered as the representative energy. Then, a Pixel-based Attenuation Matrix (PAM) was computed for each representative energy by applying Inverse Radon transform to the associated Sinogram. We also calculated the normalized photon flux of each interval to use it as a weighting factor. When we calculate the Hounsfield unit scale (HU) for each interval's representative energy, we used PAM and the normalized photon flux to modify the CT image.

The performance of the proposed method was demonstrated through Complexity and Visual analysis. Entropy measurements, Kolmogorov complexity, and morphological richness were calculated to evaluate the complexity. Calculating morphological richness (MR) for the post-processed CT images at different energy levels shows that the proposed post-processing method can better uncover the tissue differentiation. Quantitative visual criteria (i.e., PSNR, FSIM, SSIM, and MSE) were reported to show the effectiveness of fuzzy C-means approach in segmenting task. These criteria show a better segmentation performance over post-processed CT images in the majority of energy levels. This in-

dicates that better tissue discrimination has been reached as the result of applying the proposed post-processing method. Therefore, using this method in clinical set up can result in a lower degree of irradiation and less tissue damage.

Acknowledgments Andrew Adamatzky was partially supported by EPSRC grant EP/P016677/1. David Masip was partially supported by TIN2015-66951-C2-2-R, RTI2018-095232-B-C22 grant from the Spanish Ministry of Science, Innovation and Universities (FEDER funds), and NVIDIA Hardware grant program.

References

[1] Cabral, B., Cam, N. and Foran, J.: Accelerated volume rendering and tomographic reconstruction using texture mapping hardware, *Proc. 1994 symposium on Volume visualization*, pp.91–98, ACM (1994).
[2] Chen, S., Liu, H., Hu, Z., Zhang, H., Shi, P. and Chen, Y.: Simultaneous Reconstruction and Segmentation of Dynamic PET via Low-Rank and Sparse Matrix Decomposition, *IEEE Trans. Biomedical Engineering*, Vol.62, No.7, pp.1784–1795 (2015).
[3] Chen, Y., Yin, F.-F., Zhang, Y., Zhang, Y. and Ren, L.: Low dose CBCT reconstruction via prior contour based total variation (PCTV) regularization: A feasibility study, *Physics in Medicine & Biology*, Vol.63, No.8, p.085014 (2018).
[4] Cierniak, R.: *X-ray computed tomography in biomedical engineering*, Springer Science & Business Media (2011).
[5] Cover, T.M. and Thomas, J.A.: *Elements of information theory*, John Wiley & Sons (2012).
[6] Dehshibi, M.M., Sourizaei, M., Fazlali, M., Talaee, O., Samadyar, H. and Shanbehzadeh, J.: A hybrid bio-inspired learning algorithm for image segmentation using multilevel thresholding, *Multimedia Tools and Applications*, Vol.76, No.14, pp.15951–15986 (2017).
[7] Duan, Y., Bouslimi, D., Yang, G., Shu, H. and Coatrieux, G.: Computed Tomography Image Origin Identification based on Original Sensor Pattern Noise and 3D Image Reconstruction Algorithm Footprints, *IEEE Journal of Biomedical and Health Informatics*, Vol.21, No.4, pp.1039–1048 (2017).
[8] Gan, G., Ma, C. and Wu, J.: *Data clustering: Theory, algorithms, and applications*, Siam (2007).
[9] Gholami, N.: Physical feature vector based on X-ray spectrum evaluation to classify CT images (in Persian), Master's thesis, Science and Research Branch, Islamic Azad University, Tehran, Iran (2015).
[10] Herman, G.T.: *Fundamentals of computerized tomography: Image reconstruction from projections*, Springer Science & Business Media (2009).
[11] Jan, S., Santin, G., Strul, D., Staelens, S., Assié, K., Autret, D., Avner, S., Barbier, R., Bardiès, M., Bloomfield, P.M., Brasse, D., Breton, V., Bruyndonckx, P., Buvat, I., Chatziioannou, A.F., Choi, Y., Chung, Y.H., Comtat, C., Donnarieix, D., Ferrer, L., Glick, S.J., Groiselle, C.J., Guez, D., Honore, P.-F., Kerhoas-Cavata, S., Kirov, A.S., Kohli, V., Koole, M., Krieguer, M., van der Laan, D.J., Lamare, F., Largeron, G., Lartizien, C., Lazaro, D., Maas, M.C., Maigne, L., Mayet, F., Melot, F., Merheb, C., Pennacchio, E., Perez, J., Pietrzyk, U., Rannou, F.R., Rey, M., Schaart, D.R., Schmidtlein, C.R., Simon, L., Song, T.Y., Vieira, J.-M., Visvikis, D., de Walle, R.V., Wieërs, E. and Morel, C.: GATE: A simulation toolkit for PET and SPECT, *Physics in Medicine and Biology*, Vol.49, No.19, pp.4543–4561 (2004).
[12] International Commission on Radiation Units and Measurements: *Tissue substitutes in radiation dosimetry and measurement*, International commission on radiation units and measurements (1989).
[13] Pincus, S.M., Gladstone, I.M. and Ehrenkranz, R.A.: A regularity statistic for medical data analysis, *Journal of Clinical Monitoring*, Vol.7, No.4, pp.335–345 (1991).
[14] Richman, J.S. and Moorman, J.R.: Physiological time-series analysis using approximate entropy and sample entropy, *American Journal of Physiology-Heart and Circulatory Physiology*, Vol.278, No.6, pp.H2039–H2049 (2000).
[15] Rueda Toicen, A.: Block Decomposition in Small Turing Machine. (2019).
[16] Scott, D.W.: On optimal and data-based histograms, *Biometrika*, Vol.66, No.3, pp.605–610 (1979).
[17] Soler-Toscano, F., Zenil, H., Delahaye, J.-P. and Gauvrit, N.: Calculating Kolmogorov complexity from the output frequency distributions of small Turing machines, *PloS One*, Vol.9, No.5, p.e96223 (2014).
[18] Taghipour, N., Javadi, H.H.S., Dehshibi, M.M. and Adamatzky, A.: On Complexity of Persian Orthography: L-Systems Approach, *Complex Systems*, Vol.25, No.2, pp.127–156 (2016).
[19] Wang, T., Nakamoto, K., Zhang, H. and Liu, H.: Reweighted Anisotropic Total Variation Minimization for Limited-Angle CT Reconstruction, *IEEE Trans. Nuclear Science*, Vol.64, No.10, pp.2742–2760 (2017).
[20] Xu, J., Zhao, Y., Li, H. and Zhang, P.: An Image Reconstruction Model Regularized by Edge-preserving Diffusion and Smoothing for Limited-angle Computed Tomography, *Inverse Problems*, Vol.35, No.8, pp.1–34 (2019).
[21] Zenil, H., Hernández-Orozco, S., Kiani, N., Soler-Toscano, F., Rueda-Toicen, A. and Tegnér, J.: A decomposition method for global evaluation of Shannon entropy and local estimations of algorithmic complexity, *Entropy*, Vol.20, No.8, p.605 (2018).

Neda Gholami received her M.S. degree in Medical Radiation engineering from Islamic Azad University in 2015 and joined Pattern Research Center in 2016. Her research interests are medical imaging and medical data processing.

Mohammad Mahdi Dehshibi the founder of Pattern Research Center, received his Ph.D. in computer vision form I.A.U, Tehran, Iran. He has been actively contributed to research topics in machine vision/learning. In 2018, he joined SUNAI group at Universitat Oberta de Catalunya as a research fellow. He has contributed to 50+ papers published in scientific Journals or International Conferences.

Andrew Adamatzky is Professor of Unconventional Computing and Director of the Unconventional Computing Laboratory, Department of Computer Science, UWE Bristol, UK. He does research in molecular computing, reaction-diffusion computing, collision-based computing, cellular automata, massive parallel computation, complexity, collective intelligence and robotics, and future and emergent computation. He authored and co-authored seven books and more than 300 papers in top-tier journals of the field. He is founding EiC of "J of Cellular Automata" and "J of Unconventional Computing" and EiC of "J Parallel, Emergent, Distributed Systems" and "Parallel Processing Letters".

Antonio Rueda-Toicen received his M.S. degree in Bio-engineering from Central University of Venezuela, Caracas, Venezuela, in 2017 and visited the Algorithmic Dynamics Lab, Center for Molecular Medicine, Karolinska Institute as a research programmer in 2018. His research interest is biomedical computer vision.

Hector Zenil co-leads the Algorithmic Dynamics Lab at the Karolinska Institute in Stockholm, Sweden. He also leads the Algorithmic Nature Group, the Paris-based lab. Before joining the Department of Computer Science at the University of Oxford as Senior researcher and faculty member he was a researcher at the Behavioural and Evolutionary Theory Lab at the University of Sheffield. He is also the current director of Oxford Immune Algorithmics, the Managing Editor of Complex Systems, and member of the editorial board of journals and book series such as the Springer series on "Emergence, Complexity and Computation," the journals Entropy, Information, Philosophies, and Frontiers in Robotics and AI.

Mahmood Fazlali received M.S. degree (2004) and Ph.D. (2010) in computer architecture from the University of Isfahan and Shahid Beheshti University (SBU), respectively. He joined the department of computer science at SBU as an assistant professor in 2012. His research interest includes parallel processing on many-core systems, re-configurable computing, and digital synthesis. Mahmood has contributed to more than 40 papers published in International conferences and peer-reviewed journals.

David Masip is professor in the Computer Science Multimedia and Telecommunications Department, Universitat Oberta de Catalunya (UOC) since February 2007, and since 2015 the director of the UOC Doctoral School. He is the director of the SUNAI (Scene Understanding and Artificial Intelligence) research group. He is member of the BCN Perceptual Computing Lab. He studied Computer Science in the Universitat Autonoma de Barcelona, obtaining a FPI grant in 2001 for starting his Ph.D. degree in the Computer Vision Center (Spain). He obtained the Ph.D. degree in September 2005 and the best thesis award on Computer Science in the Universitat Autonoma de Barcelona.